Published in : Optics & Laser Technology (2023), vol. 163, 109426
DOI: 10.1016/j.optlastec.2023.109426
Status : Postprint (Author's version)

OPTIMIZING LASER POWER OF DIRECTED ENERGY DEPOSITION PROCESS FOR HOMOGENEOUS AISI M4 STEEL MICROSTRUCTURE

Rúben Tome Jardin[a], Víctor Tuninetti[b],*, Jerome Tchoufang Tchuindjang[c], Laurent Duchene[a], Neda Hashemi[c], Hoang Son Tran[a], Raoul Carrus[d], Anne Mertens[c], Anne Marie Habraken[a,e,*]

[a] *Department ArGEnCo-MSM, University of Liege, Liège 4000, Belgium*
[b] *Department of Mechanical Engineering, Universidad de La Frontera, Temuco 4780000, Chile*
[c] *Department A&M-MMS, University of Liege, Liège 4000, Belgium*
[d] *Sirris Research Centre (Liege), Seraing 4102, Belgium*
[e] *Fonds de la Recherche Scientifique-F.R.S.-F.N.R.S., Brussels 1000, Belgium*

* *Corresponding authors at: Department of Mechanical Engineering, Universidad de La Frontera, Temuco 4780000, Chile (V. Tuninetti). Department ArGEnCo- MSM, University of Liege, Liège 4000, Belgium (A.M. Habraken).*

E-mail addresses: victor.tuninetti@ufrontera.cl (V. Tuninetti), anne.habraken@uliege.be (A.M. Habraken).

KEYWORDS: Finite element modeling -- Numerical optimization -- Additive manufacturing -- Directed energy deposition -- Melt pool size -- Nanohardness map

ABSTRACT

A finite element model of directed energy deposition (DED) process predicts the thermal history during the manufacturing of high speed steel cuboid samples. The simulation result validation relies on comparisons between measured and predicted data such as temperature histories within the substrate and the melt pool depth of the last coating layer. Integrated within an optimization loop, these DED simulations identify two variable laser power functions able to generate a constant melt pool size. These functions are expected to provide a homogeneous microstructure over layers. The computed thermal fields and the microstructure generated by three AISI M4 experiments performed with the constant laser power case and the two optimized functions at three points of interest located at different depths within the deposit are correlated. The effect of the melt superheating temperature and the thermal cyclic history on micro and nanohardness measurements is observed. As a result, the optimized laser power functions provide samples with more homogeneous microhardness than the constant laser power function, however, the homogeneity of microstructure is not fully confirmed by the nanohardness map throughout the deposited M4 steel layers.

Published in : Optics & Laser Technology (2023), vol. 163, 109426
DOI: 10.1016/j.optlastec.2023.109426
Status : Postprint (Author's version)

1. Introduction

To overcome the challenges related to increasing carbon emissions, noise and energy consumption in air transportation product development and related manufacturing industry, additive manufacturing (AM) processes are considered one of the best emerging technologies contributing to the fourth industrial revolution. The different AM technologies produce components with special or complex metal alloys, flexible and functional designs, and consequently light weight [1-5]. In addition, the associated AM repair technology also contributes to increase service life by recovering damaged components [6].

The two main known groups of AM technologies are directed energy deposition (DED) [7-14] and powder bed fusion (PBF) processes [15-19]. Some advantages of DED process over PBF (laser (L-PBF) or electron beam (EB-PBF)) are their high versatility and controllability, increased build rates and volumes, and lower material powder required [20]. PBF processes generally allow building high resolution parts [21]; while DED processes are generally suitable for near net shape products, cladded parts operating in extreme conditions, and repaired high-valued components [6,22]. The current study is focused on improving DED part quality by optimizing the laser power function thanks to 2D finite element (FE) simulations. The optimal laser power functions identified are expected to produce parts with improved homogeneity, which will be evaluated at the microscopic level by Vickers profiles and nanoindentation mapping.

AISI M4 high speed steel grade shows a high potential of wear properties (Fig. 1). The AISI M4 wear behavior of DED samples is strongly related to the size and the distribution of both vanadium-rich MC carbides and molybdenum-rich M_2C carbides present at cell boundaries. This statement is confirmed in Hashemi et al. [23], which compares the wear behavior of different high speed steel grades (DED cuboid deposits of 30-35 mm square and 20-25 mm high versus cast samples). DED ultrafine and cellular-type microstructures (Fig. 2(a) and 2(b)) containing rounded shape M_2C carbides lead to low wear rates (see Fig. 2) compared to coarser microstructures (note the different image scale) obtained under conventional casting route (Fig. 1(c)). This cast image contains both large MC carbides inside grains and acicular M2C carbides at grain boundaries. In addition, the top layer within DED sample has a slightly finer microstructure than the core layer as mentioned in the previous work of Jardin et al. [24]. This fact could explain why the wear rate is also slightly lower close to the DED surface compared to the bulk for DED samples at low sliding speed but does not justify the higher wear rate for higher sliding speed. Nevertheless, the wear rate within DED samples is clearly less sensitive to sliding speed compared to conventional casting, regardless of the location within the thick deposit. This fact points a higher homogeneity within the structure at a macro scale for DED samples, while the non-constant wear properties with the height location still suggests a heterogeneity of the microstructure that could be improved.

The homogeneity issues within DED samples is not new. For instance, Shim et al. [7] developed a process diagram to relate the single-layer height to the specific energy density and the powder feed density in order to improve geometric accuracy and mechanical properties of the final part of high-

Published in : Optics & Laser Technology (2023), vol. 163, 109426
DOI: 10.1016/j.optlastec.2023.109426
Status : Postprint (Author's version)

speed-tool steel AISI M4. Their results concluded that a time-varying energy supplied to the melting zone affects the cooling rate and the solidification rate of the deposited layers, resulting in an inhomogeneous micro-hardness throughout the deposited region. The nonuniform micro-hardness was explained by variation in the grain size and the martensite fraction at each location of the deposited region, caused by the history of the energy input in the material. It indeed generates a non-uniform solidification rate of the AISI M4 steel. In addition, Shim et al. [25] studied the effect of substrate preheating by induction heater on DED AISI M4 powder. Their results indicated that the process parameters such as laser power, powder feed rate, and induction energy should be cautiously designed to limit the melting pool rise, which resulted in an over-deposition leading to a dimensional error.

Note that the microstructure heterogeneity is not the single peculiarity observed in DED samples. Within additive parts, there are also for instance uncontrolled voids, micro-cracks, part distortions and surface roughness [26-28] which are not present in wrought materials [26,29,30]. Among the numerous process parameters conditioning the feasibility of a DED part are the laser power and spot size, powder flow and composition, scanning speed, working distance, hatch spacing and overlap, scanning and slice strategy. To increase the part quality, online process monitoring and control have been applied to variate the temperature of the melt pool, its size, the deposition thickness and the powder flow. Forinstance, Su et al. [31] proposed a closed-loop control method based on the proportional integration algorithm (PID) to enhance the wear resistance by tuning and controlling in real time the laser power and molten pool size. Closed-loop melt pool size reduction control affects the cooling rate, promotes phase transformation and grain refinement, consequently increasing the deposited part strength [32]. Cong and Ning [33] proposed an ultrasonic vibration for the DED process to reduce voids and cracks, achieving improved geometrical and microstructural characteristics, and consequently higher mechanical resistance in stainless steel parts. Park et al. [34] developed a real-time Poisson's ratio and Young's modulus estimation technique for the DED process using femtosecond laser ultrasound. For process repeatability, quality measurement of the nozzle geometry variation during service life due to scouring erosion of the inner channel in contact with the highspeed powder particles must be considered as reported by Tan et al. [35]. The complexity of obtaining accurate geometry has been reported by Peng et al. [36], while other researchers have been focused on the path strategies effecting the properties and the geometrical dimensions of the manufactured parts. Woo et al. [37] examined the through thickness microstructure, the thermal and mechanical properties, and the residual stresses of a DED functionally graded steel (FGM) specimens finding an equiaxed grain structure created by the epitaxial grain growth along the building direction with a maximum significant variation of 950 MPa of residual stresses. The stresses were released to about 430 MPa when the FGM were manufactured with orthogonal or island (chessboard) interlayers scanning strategies. In Biegler et al. [38], two different path-planning strategies for AISI 316L bulky parts such as the contour-parallel and the zig-zag were compared. The characteristic errors observed at curved and narrow areas for the zig-zag strategy and at sharp angles for the contour-parallel strategy demonstrated that the performance of path is highly geometry dependent.

Published in : Optics & Laser Technology (2023), vol. 163, 109426
DOI: 10.1016/j.optlastec.2023.109426
Status : Postprint (Author's version)

Figure 1. *Wear properties of AISI M4 DED and casted samples under two different sliding speeds and for DED, at the sample surface associated with the last deposit layer and in the core sample.*

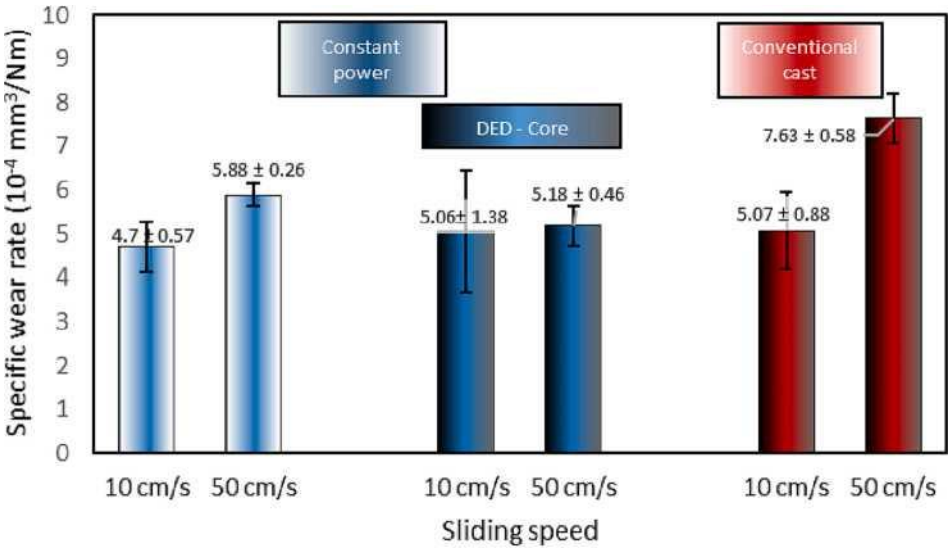

In addition to the tools and techniques developed to improve the quality of DED process listed here above, numerous experimental and numerical researches have been specifically conducted on the links between thermomechanical properties, process parameters and microstructure features of the deposited material [26,39-42]. For Ti6Al4V material, in Lu et al. [43] the microhardness and tensile property of the specimens obtained by DED were significantly improved by the interlayer laser shot peening treatment, reaching properties equivalent to those found in raw Ti-6Al-4 V [44]. Razavi et al. [26] pointed the higher cycle fatigue strength in DED versus forged samples, with differences attributed to grain size. In Tran et al. [40], a correlation between the microstructure and the temperature evolution was obtained from finite element thermal simulations of DED process of Ti6Al4V alloy. While for steels produced by DED process, Guan et al. [45] characterized the effect of the laser incident energy on the morphology of microstructures of 12CrNi2Y alloy steel. Bertsch et al. [46] found that thermal distortions during additively manufacturing of austenitic stainless steel 316L are the primary reason of the dislocation structures, which are dependent on the constraints surrounding the melt pool and the thermal cycling.

Finally, according to the state of the art presented in C. Wang et al. [20], additive manufacturing coupled with machine learning can improve the development of new high-performance materials, thanks to the optimization of topological designs or process parameters, as well as the analysis of on line process for defect monitoring. Zhang et al. [47] applied two machine learning algorithms to predict melting pool temperature in a DED process with high accuracy. However as pointed by Pham et al. [48,49] an accurate deep learning strategy requires significant experimental data or validated finite element simulation results of the process to generate accurate predictions. In Pham et al. [48], a simple FFNN architecture was applied to model DED manufacturing of AISI M4 samples. The developed surrogate model was 180 times quicker than a FE simulation and it allowed to perform an uncertainty quantification and sensitivity analysis of M4 DED sample manufacturing process. The results confirmed that convection, laser power, scanning speed, and conductivity induce the most uncertainties in melting pool sizes [49].

Published in : Optics & Laser Technology (2023), vol. 163, 109426
DOI: 10.1016/j.optlastec.2023.109426
Status : Postprint (Author's version)

Based on previous literature review, it is clear that the most relevant process parameters concerning the heat input are laser power, powder flow rate, scanning speed and spot size. In the current research, the aforementioned parameters were first kept constant in the manufacturing of DED cuboid sample manufactured from M4 steel powder. It allowed validating the FE predicted thermal field history versus the temperature measured at the local points [24]. The fact that the melt pool size is highly sensitive to the laser power function explains why the current article is focused on this process parameter. Indeed, the solidification process determines the microstructure which controls the material properties. A constant melt pool size should provide constant homogeneous material properties if no further external parameters disturbs the system. Hereafter, an optimization loop varies the laser power to achieve a homogeneous microstructure thanks to a constant melt pool size. M4 bulk parts manufactured by DED with constant and optimized laser power functions are compared. To validate the proposed methodology to reach a homogeneous microstructure, nano indentation hardening mappings and images of optical and scanning electron microscopy are performed. They are corroborated by macro hardness

profile throughout the sample.

The present article is organized as follows. Section 2 describes the manufacturing process, the fabricated parts, as well as the strategy of power optimization. Section 3 provides the numerical model of the DED process, while Section 4 present the results related to the different laser power functions: molten pool sizes and temperature histories, as well as the experimental micro and nanohardness maps of the deposited materials with their respective analysis. The main conclusions and ongoing work are listed in the last Section 5.

Figure 2. *SEM micrographs (BSE) show the ultrafine and cellular-type microstructures of DED AISI M4 sample manufactured with a constant laser power, (a) near the surface (within top layer), (b) at the sample mid height, and (c) BSE images of the coarse microstructure of a conventional cast sample (note the lower magnification of c image versus a and b ones).*

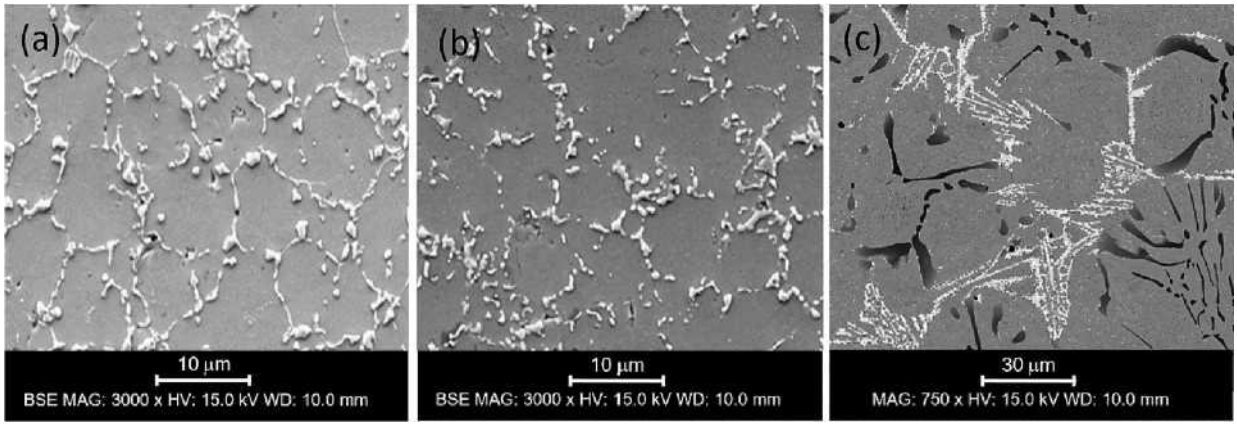

Published in : Optics & Laser Technology (2023), vol. 163, 109426
DOI: 10.1016/j.optlastec.2023.109426
Status : Postprint (Author's version)

2. Materials and methods

2.1. MANUFACTURING PROCESS

The schematic depiction of the DED process applied to manufacture the M4 samples is shown in Fig. 3(a). The 5-axis 2 kW Irepa Nd-YAG laser DED machine of Sirris Research Center was used to manufacture three rectangular cuboids from M4 high speed steel powder of 50 to 150 µm particle size (Table 1). The top-hat intensity distribution laser beam spot diameter is 1.5 mm. Overlapping tracks of 1.4 mm were applied and Argon gas was utilized for the protection of the workpiece. The processing head of the machine is equipped with a coaxial supply of powder to the laser beam in order to apply the powder with 10 mm of standoff distance (substrate surface distance from the nozzle tip).

Three different laser power functions were considered for manufacturing the three types of samples, one constant power value (CP) and two time dependent functions: LPF1 and LPF2, which were identified by the method described in Section 2.3. The process parameters such as the nozzle scanning speed, powder feed rate, and the preheating temperature of the 42CrMo4 substrate (40 mm height, 100 mm diameter) were set constants with 6.87 mm/s, 76 mg/s, 300 ° C, respectively. The dimensions of the manufactured samples and the locations of hardness measurements are given in Table 2. The temperature points recorded during the process by 4 thermocouples were located within the substrate at a depth of 5 mm from the top surface and at a distance of 20 mm from the substrate circumference. The clad sample geometry and axes are described in Fig. 3(b) while Table 2 provides the accurate dimensions.

2.2. HARDNESS MEASUREMENT CAMPAIGN

The mechanical properties such as yield limit can be related to Vickers hardness profiles. Table 2 gives the Vickers measurement locations and Fig. 8(b) the hardness profiles. Vickers hardness measurements are performed on a universal EMCO MC10 machine equipped with an electronic cell force and a closed loop regulation, using a load of 100 N.

For each sample, a hardness profile is made along a line parallel to the building direction (Z axis) and close to the middle of the block (see Table 2). There is one Vickers indent every 500 µm starting from the top of the deposit down to the substrate. The Vickers hardness measurements (Fig. 8) help determining the evolution of the homogeneity of the structure at a macro scale in the core of the sample.

Nanoindentations tests are carried out using a Hysitron Ti 950 Triboindenter with a Berkovich tip. The nano indentation grid locations are provided in Fig. 8(a) and the measured nanohardness maps are reported in Fig. 9 for the three samples. Each 46x36 grid results in 1656 indents, with 3 µm between two consecutive indents. The tests are performed under displacement control mode; the penetration depth being set at 300 gm for each indent. The nanoindentation tests are intended to assess the homogeneity of the microstructure at a local scale.

Published in : Optics & Laser Technology (2023), vol. 163, 109426
DOI: 10.1016/j.optlastec.2023.109426
Status : Postprint (Author's version)

2.3. MICROSTRUCTURE CHARACTERIZATION

The microstructure of the manufactured sample with a constant laser power (CP) was characterized at the top and middle points located at 760 µm and 13.8 mm from the upper free surface of the DED sample respectively (Fig. 4). Two magnifications of 1000 x and 3000 x are used to observe a cellular-type microstructure with slightly varying size between the different layers. As established in Jardin et al. [9], the apparent scratches seen under high magnification should be related to residual austenite not transformed into martensite in this as built sample. Similar images were measured for samples generated by LPF1 and LPF2.

Figure 3. *(a) DED process used for the manufacturing of the bulk M4 samples, (b) Cuboid sample geometry and axes.*

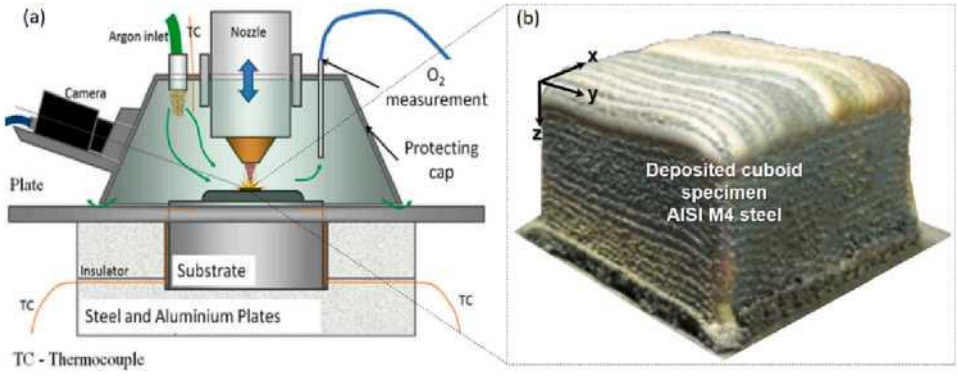

Table 1. *Mass fraction of feedstock M4 powder steel used for the DED AM of cuboid samples.*

W	Mo	Cr	V	C	Ni	Mn	Si	Fe
0.0560	0.0464	0.043	0.0410	0.0135	0.0090	0.0034	0.0033	Bal.

Table 2. *Geometry of the M4 steel DED manufactured cuboid parts including Vickers hardness measurements locations.*

Cuboid parts	Total height (Z direction, mm)	Width (X direction, mm)	Length (Y direction mm)	Vickers Hardness profile length	Position of Vickers Hardness profile within deposit	
					X (mm)	Y (mm)
Constant power (CP)	27.3	41.5	42	15.5	17.6	21.5
Function 1 (LPF1)	20.8	41.9	43.4	20.5	22.4	22.1
Function 2 (LPF2)	23.6	41.6	43.1	20.5	20.8	19.2

Published in : Optics & Laser Technology (2023), vol. 163, 109426
DOI: 10.1016/j.optlastec.2023.109426
Status : Postprint (Author's version)

Figure 4. *Microstructure of cuboid sample manufactured with constant DED laser power observed at top and middle locations with two magnifications 1000x and 3000 x.*

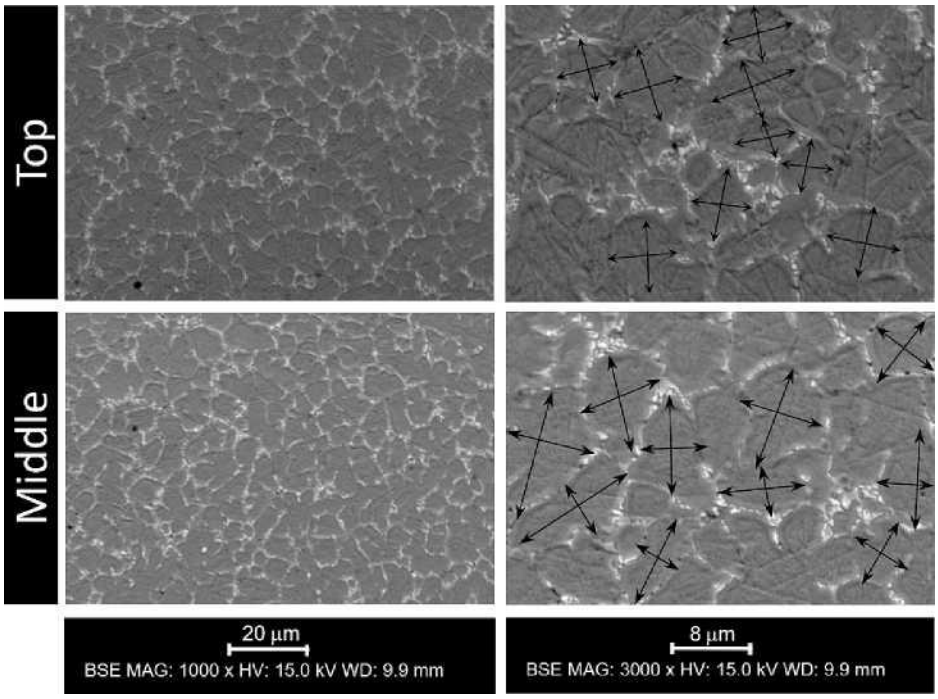

3. Numerical model of the DED process

This section presents the finite element simulations of the DED process as well as the Python script computing the optimization of the laser power functions to achieve a melt pool of constant size within the deposit height.

3.1. FE SIMULATION OF DED PROCESS

The Lagamine FE code developed since 1984 [50-54] at the University of Liege is used to compute the thermal history of the deposit and the substrate. The Fourier's law of heat conduction, and the surface energy balance considering convection and radiation heat transfer equations are taken into account within the two dimensional FE simulations. The model relies on the BLZ2T solid finite element and the CONRA interface elements (see Lagamine user guide for details [54]). The addition of material during the additive process is simulated by using the element birth technique [40]. Further information of the numerical modeling and previous simulations of the investigated AISI M4 DED process are given in Jardin et al. [24].

The FE model shown in Fig. 5(a) considers a vertical cut in the center of the deposit material. The horizontal and vertical mesh directions of the zoom picture in Fig. 5(a) are aligned with the horizontal trajectory of the laser and the building direction respectively. In order to reduce the computational time, the 36 deposited layers of an average size of 0.764 mm height are modeled with bidimensional elements assuming no transversal thermal flow outside the mesh plane. Such an

Published in : Optics & Laser Technology (2023), vol. 163, 109426
DOI: 10.1016/j.optlastec.2023.109426
Status : Postprint (Author's version)

assumption can be questionable but allows reasonable CPU time which is a mandatory constraint as an optimization loop is aimed. The implication of this 2D choice is a careful definition of the boundary conditions that are adjusted to recover both the measured thermocouple histories and the melt pool size measurements. Validations of this simplified approach for the studied sample geometry has been provided both for AISI M4 material [24] and for 316L + WC [55]. To generate an optimal 2D FE mesh, transition refinement element groups are used and the nonuniform mesh refinement given in Fig. 5(a) is applied. The substrate affected by the laser source is refined to accurately model heat fluxes, while the bottom of the substrate is coarsely meshed. The heat flux loading under the laser beam is applied to 2 solid elements by nodal power values and convection and radiation interface elements are placed on the boundaries of the substrate and the deposit to model the heat exchanges. Inside the deposit, the element width of 0.75 mm corresponds to half of the diameter of the laser spot. Applying the laser beam speed used in the experiment, the element birth technique of the 2D FE simulation models the movement of the heat source and material addition with an idle time taking into account the missing tracks not computed for each layer. For the simulations, the laser heat flux scale factor between the 2D model and the experiment with a constant laser power was adjusted based on the measured substrate temperature and the melt pool size of the last layer. Such a double check is mandatory to prevent any lack of representativeness of the simulations [56]. In the 2D FE model of DED process, the physical laser power value and the absorptivity factor can indeed not be directly used [57].

The variations of thermal conductivity, density and specific heat capacity with the temperature were measured from specimens extracted from the deposit and from substrate [9]. Regarding the emissivity factor for radiation and convection coefficient, values of 1 and 230 W/m^2K, are respectively used. It is worth mentioning that thermodynamic simulations (Calphad) allowed obtaining the solidus and liquidus temperatures corresponding to 1503 K and 1677 K for AISI M4 materials. According to Morch et al. [58], for the numerical stability and physical accuracy of the predicted temperature fields, a continuous evolution of the thermophysical material properties over the process temperature range is essential, a feature that was respected in the input material data set.

Published in : Optics & Laser Technology (2023), vol. 163, 109426
DOI: 10.1016/j.optlastec.2023.109426
Status : Postprint (Author's version)

Figure 5. *(a) 2D FE Mesh used for DED process simulations and (b) flowchart of the laser power optimization process strategy for a constant melt pool size.*

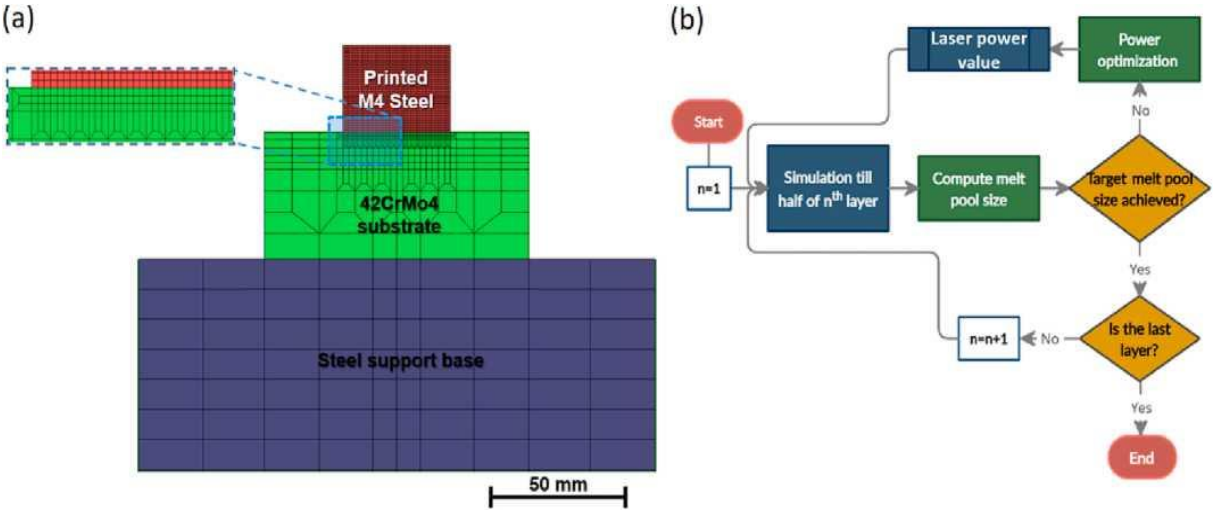

3.2. OPTIMIZATION STRATEGY TO REACH A CONSTANT MELT POOL SIZE

Within a Python script, at each new layer, the value of the laser power assumed constant within the layer is adjusted to predict the constant melt pool size (depth and length) requested by the user. This optimization loop, based on a Newton-Rapson iterative method modifies the input laser power value to minimize an objective function expressing the difference between the user constant values requested and the ones computed. The flowchart of this optimization scheme is shown in Fig. 5 (b).

4. Results and discussion

The microstructure of metals and alloys are highly dependent on the thermal gradient, solidification temperature gradients and cooling rates. For the manufacturing of DED samples, the process parameters determine the thermal cycles and the number of re-melting of each layer which affects the homogeneity of the local material properties near the melt pool boundary. Based on two different runs with different targets, the optimization Python script strategy based on the 2D FE DED process model has determined two laser power functions (LPF1 and LPF2). The experimental results compare the microstructure homogeneity of the samples generated by these functions with the one manufactured with a constant laser function (CP).

4.1. LASER POWER FUNCTIONS, MOLTEN POOL SIZES AND TEMPERATURE HISTORIES

Iterative steps varying the laser power value associated to each layer of the simulated DED samples are run in order to reach a constant melt pool size (length and depth). Numerical results of the melt pool size by applying a constant power value and the identified optimized laser power functions are

Published in : Optics & Laser Technology (2023), vol. 163, 109426
DOI: 10.1016/j.optlastec.2023.109426
Status : Postprint (Author's version)

shown in Fig. 6. Homogeneous melt pool depth and length are indeed numerically computed in the sample manufactured with both laser power functions LPF1 and LPF2. Each power function provides a homogeneous melt pool of a different size: 1.4 and 1.8 mm for the depth and 5.7 and 4.4 for the length, respectively; which were the two different targets within the optimization process.

Regarding the computed thermal history, the peak values of three typical observed zones (Bottom, Middle, Top) in Fig. 7 are different for each power function (CP, LPBF1, LPBF2). As in Jardin et al. [24], the 2D finite element mesh (Fig. 5(a)) models the center track of each layer of the actual process and the FE simulations provide the thermal field at any point in this middle plane. The temperature histories of the material points representative of the Bottom, Middle and Top of the samples (see Fig. 8(a)) and deposited in the middle plane of the sample are plotted in Fig. 7 for each power function (CP, LPF1, LPF2). Each curve shows the temperature observed by a material point: a peak above the melting temperature while the material is deposited, followed by a cooling stage as the laser moves away. The first rapid local cooling is due to solidification energy, followed by a slower gradient due to heat loss to the workpiece by conduction and to the surroundings by radiation and convection, when the laser moves away. When the next layer is deposited, there is a warming as the laser approaches and the material point is melted a second time but its temperature level is lower and a cooling stage happens again as the laser moves away. This thermal cycle repeats itself being attenuated more and more (partial then no re-melting), as more and more layers separate the analyzed material point from the laser energy source. For the Bottom representative point, the effect of the last layers is not any more noticeable (no peak). The Top representative points are at the second last layer for the LPF1 and LPF2 power functions as only two peaks are observed (Fig. 7 (b) and (c)) and 2 layers deeper for the constant laser power case. Note that each sample has a different height as a different laser power values generates different layer heights which explains the different time and layer number associated to each zone in Fig. 7. The highest peaks are observed as expected in the manufactured part with the LPF2 manufacturing (highest power value), and the maximum peak values have average of 2660 K. In addition, the number of thermal cycles inducing a total remelting of a layer and the value of the temperature reached during total or partial remelting present considerable changes with the laser power energy function. This number of remelting phenomena increases with the laser power.

Both previous phenomena, superheating value and number of remeltings extracted from the simulations of the DED manufacturing process help to analyze the experimental microhardness profiles and the nanoindentation distribution maps of the samples, as well as the residual stresses state that justify post-mortem cracks discussed in the next subsection.

4.2. MICROHARDNESS DISTRIBUTION OF THE SAMPLES

Fig. 8(a) shows the cross-section of the cut samples obtained with the different laser power functions. The cutting of the sample manufactured by CP and LPF1, required for hardness measurements, revealed cracks appearance. As proved by the observations of all the as-built samples, they do not present any crack (Fig. S1). The lack of oxidation, confirmed by EDX mapping performed within the cracks present after cutting in CP and LPF1 samples tells that those cracks are

Published in : Optics & Laser Technology (2023), vol. 163, 109426
DOI: 10.1016/j.optlastec.2023.109426
Status : Postprint (Author's version)

post mortem (Figs. S2 and Figs. S3). They appeared when cutting the sample and not during the DED process. During the process, cracks would also have been noticed because of noise and of the fact that the laser DED machine is programed with a security feature which stops the process if a minimum standoff distance (between the laser and the deposit) is reached. Indeed, a crack reduces this distance and in addition, the sample shape would have also been affected due to the lower conducted heat escape. So all these reasons confirm the post mortem crack assumption. The LPF2 sample exhibits reduced residual stresses inside the cubic part built according the absence of any cracking during cutting. This LPBF2 case is interesting as it avoids further heat treatments [59] required to reduce the residual stresses generating cracks in both CP and LPF1 samples. The higher heat accumulation achieved within sample LPF2 (Fig. 7c) in comparison to samples CP and LFP1 (Fig. 7a and b), and the higher homogeneity level within the same sample can justify a better stress relief that avoids a subsequent cold cracking phenomenon.

Both the level and the scattering of the microhardness profiles provide information on the microstructure state. More homogeneous profiles with the optimized laser power functions LPBF1 and LPBF2 are obtained, at a qualitative level, according the hardness scattering features of the curves Fig. 8(b) and the computed variance (Fig. 8(c)).

Figure 6. *(a) Laser power functions obtained from the proposed methodology. (b) Computed molten pool over the layers for LPF1, LPF2 and CP.*

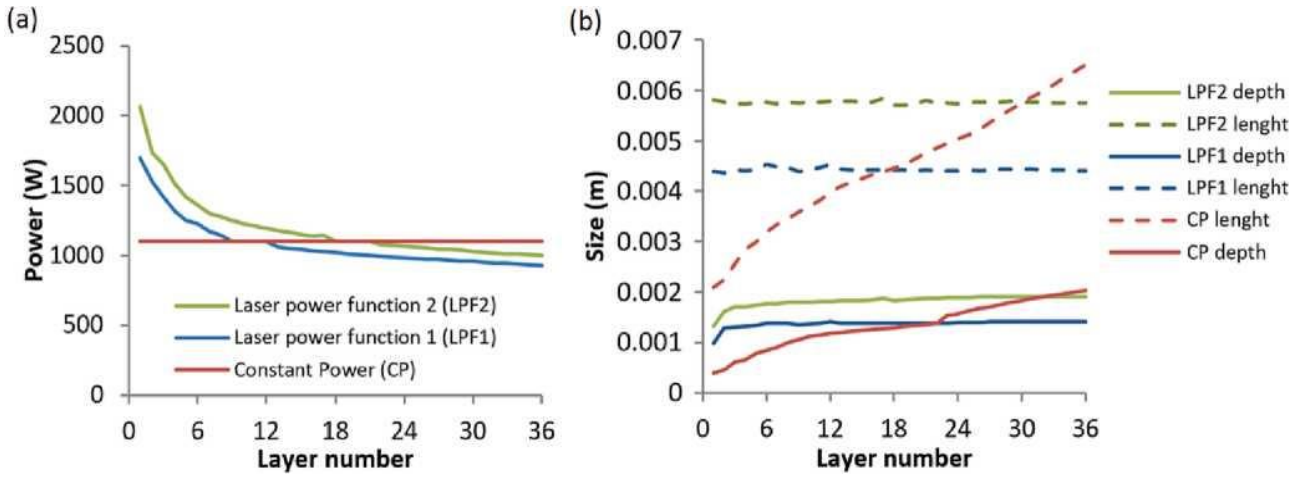

Published in : Optics & Laser Technology (2023), vol. 163, 109426
DOI: 10.1016/j.optlastec.2023.109426
Status : Postprint (Author's version)

Figure 7. *Thermal history of the Top, Middle and Bottom layers obtained by applying the three laser power functions: (a) CP, (b) optimized LPF1, and (c) optimized LPF2.*

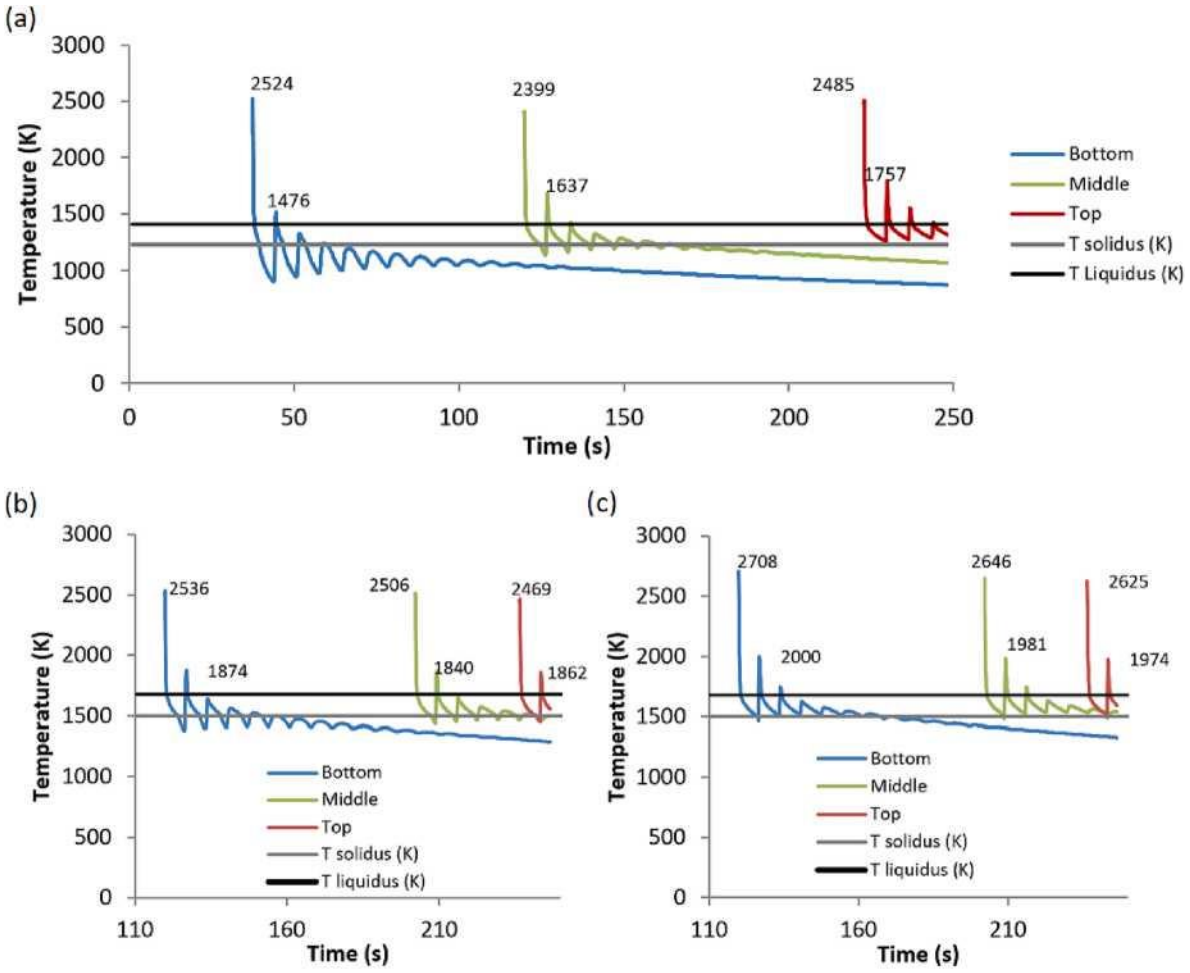

4.3. NANOMECHANICAL HARDNESS MAP

The nanoindentation grids performed in the cut sections of the manufactured samples at the location points given in Fig. 8 allow building the nanohardness maps of Fig. 9. The part manufactured with constant power (CP) shows non-homogeneous nanohardness field with higher values in the middle zone of around 9.5 GPa. A more homogeneous hardness field is found with the laser power function 1 (LPF1) compared to CP. However, the local hardness in the middle zone show higher values and variation which is not the target aim of this work. This is clearly not seen in the Vickers hardness measurements (Fig. 8) and cannot be explained by the computed thermal histories since the measurement resolution here is higher than the element size. It would require a mesh refinement which is not justified since mass transfer effects due to convection and Marangoni effect cannot be represented with the current implemented macroscopic solid finite element model. The targeted homogeneous nanohardness distribution in the Middle zone of the part are finally obtained by applying the optimized laser power function 2 (LPF2) defined by the developed optimization strategy. The reduced hardness in the top layer is actually not an issue, because the last deposited

Published in : Optics & Laser Technology (2023), vol. 163, 109426
DOI: 10.1016/j.optlastec.2023.109426
Status : Postprint (Author's version)

layer and free surfaces of the part are generally machined in order to obtain a good surface finish and accurate final shape of the manufactured part.

4.4. ANALYSIS OF RESULTS

The thermal histories shown in Fig. 7 (the maximum temperatures of the melt pools, the peak temperatures of the liquid metal during the last solidifications, the numbers of total or partial remeltings) within the top, the middle and the bottom zones of the samples, obtained by applying constant CP, optimized LPF1 and LPF2 laser power functions are analyzed to identify any links with the melt pool sizes and the micro and nanohardness profiles.

The discrepancies between the thermal histories associated to each location are clearly higher for the CP case (Fig. 7(a)) than for LPF1 and LPF2 cases, which is consistent with the computed non-constant melt pool of CP case versus LPF1 and LPF2 cases (Fig. 6(b)). For the latter cases, the very small variations around the reached constant melt pool size are similar, however the discrepancies between the thermal histories of the different location points in LPF1 case (see the numbers of remelting events between bottom and middle locations) are higher than the ones observed for LPF2. This ranking in variations within the local thermal histories of each sample is kept within the heterogeneity of their nano indentation maps (Fig. 9).

The higher homogeneity of the LPF2 part observed in nanohardness maps (Fig. 9) could be associated to the highest peak temperature values of the melt pools (the average value is 2569 K for the maximum temperature) compared to CP (2469 K) and LPBF1 (2505 K) cases. It produces a higher accumulation of heat which generates slower cooling process (see Fig. 7(c)), allowing more homogenous temperature within the parts as well as lower residual stresses. No crack appeared during the postmortem vertical cross-section inspection, provided in Fig. 8, for LPF2 case compared to CP and LPF1 cases. These cracks are the result of the critical residual stresses in the as-built conditions. The in-situ annealing during LPF2 processing helps achieving stress relief unlike in CP and LFP1 configurations.

The CP sample shows heterogeneity both at the macro level (see Vickers profile Fig. 8) and at the nano scale (Fig. 9). The average nanohardness is low at the bottom of the deposit, and more importantly, it shows some heterogeneity within the melt pool areas. For the top of the deposit, the average hardness is globally lower, even if it is more homogeneous than at the bottom. On the other hand, in the middle of the deposit, there is a higher level of hardness (average of 9.5 GPa in nanohardness and 800 HV in Vickers). Considering the previous studies, it can be noted that such a hardness for the given alloy can lead to improved mechanical [9] and tribological properties [23]. In the case of wear resistance in particular, the wear loss was found homogeneous regardless of the sliding speed within this middle location (see Fig. 1). This zone of the CP sample can therefore be considered as the adequate homogeneous structure (AHS) to achieve.

The LFP1 sample exhibits the AHS only on the top position, the middle and the bottom position being different, with higher hardness and/or a more pronounced heterogeneity. Therefore, a local

Published in : Optics & Laser Technology (2023), vol. 163, 109426
DOI: 10.1016/j.optlastec.2023.109426
Status : Postprint (Author's version)

thermal post-treatment should be required to achieve the AHS in all the zones, which is not an easy task.

The LFP2 configuration, on the other hand, presents the AHS in both the bottom and the middle positions. The top of the deposit, on the other hand, shows a slightly lower average hardness, which is however not critical if machining is considered subsequently.

Figure 8. *(a) Overview of cross-sections with the location of the vertical hardness profiles close to the middle axis for the tree manufacturing strategies of laser power function (CP, LPF1 and LPF2); (b) Evolution of the hardness profile with the depth from the top surface of the samples; and the (c) computed average values of microhardness Vickers HV_{10} measured at the cross-section.*

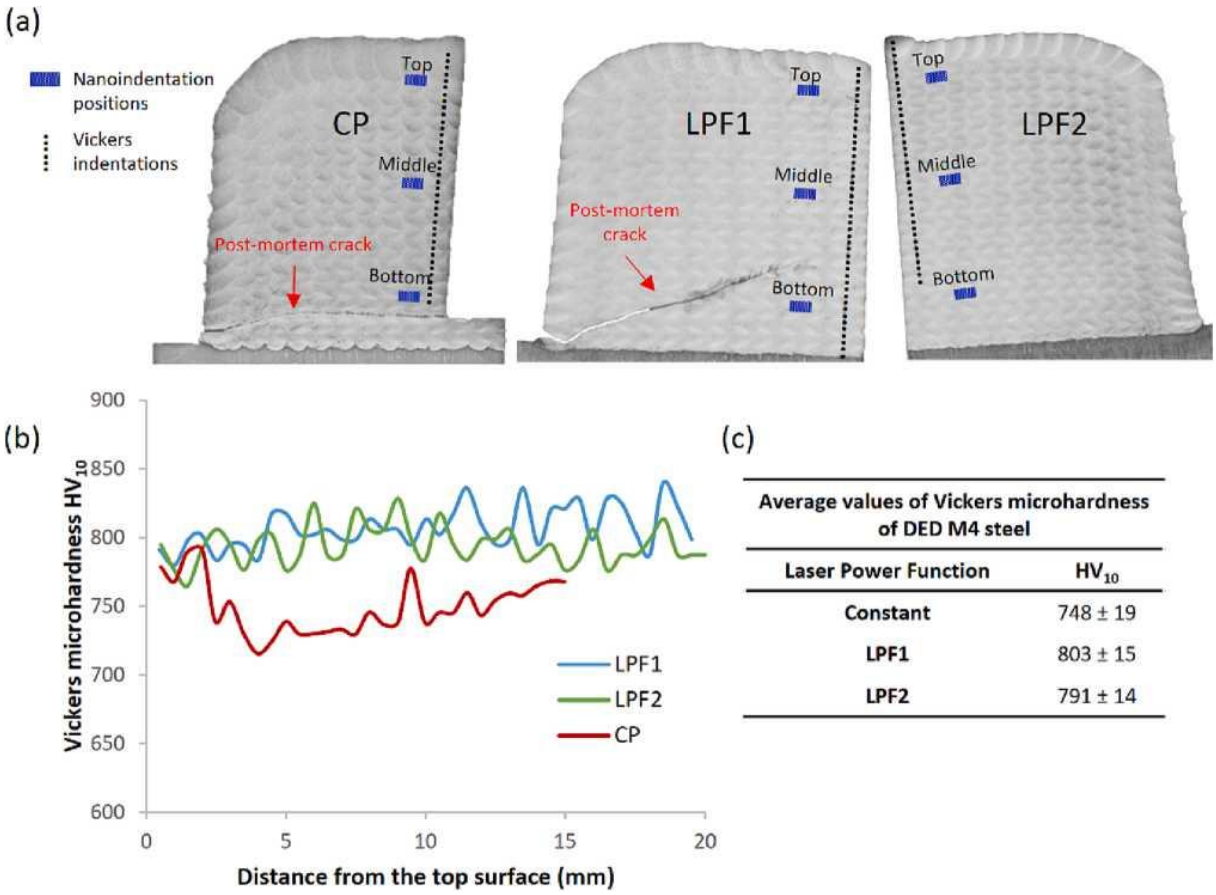

(c)

Average values of Vickers microhardness of DED M4 steel	
Laser Power Function	**HV_{10}**
Constant	748 ± 19
LPF1	803 ± 15
LPF2	791 ± 14

Published in : Optics & Laser Technology (2023), vol. 163, 109426
DOI: 10.1016/j.optlastec.2023.109426
Status : Postprint (Author's version)

Figure 9. *Nanohardness maps of the cross-section of the samples at the top, bottom and middle location points.*

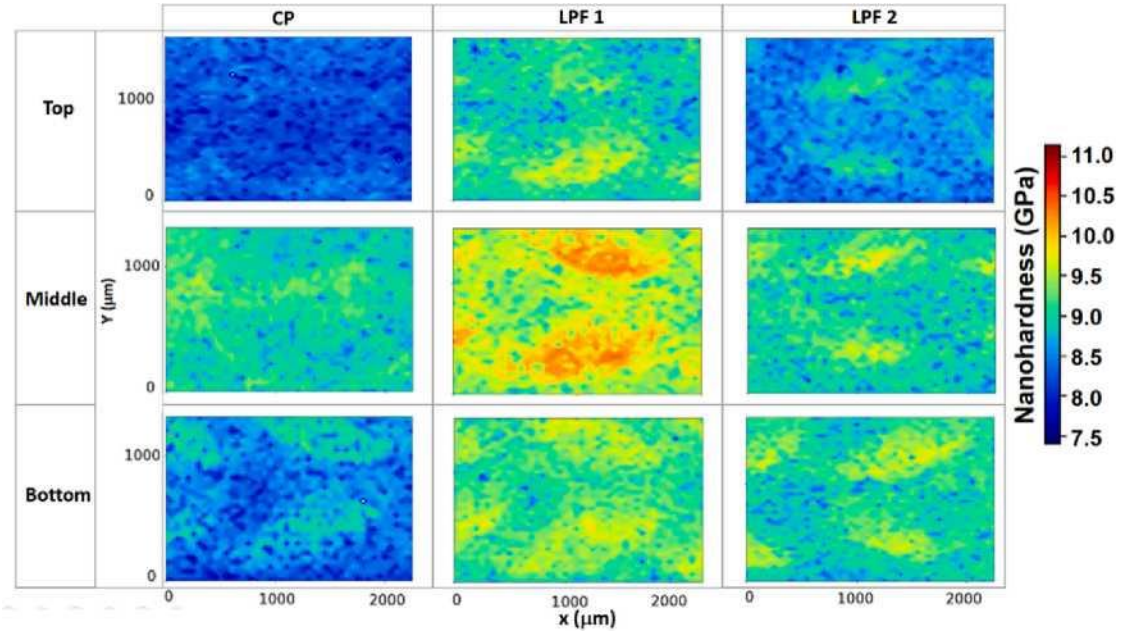

5. Conclusions

The main objective of this work was to develop a process strategy to reach homogeneous and optimal mechanical properties of the whole AISI M4 DED as built material part to avoid or reduce thermal post treatment. The numerical strategy presented here is a cost effective method for saving time and improving quality in the DED manufacturing and repair processes of machine tools and parts. Using validated 2D FE thermomechanical simulations of the DED process within a Newton-Rapson optimization method, an optimal laser power function was determined to generate bulk M4 steel samples with a constant melt pool along the built direction.

Regarding the link with the thermal history, the dimensional control of the melt pool reasonably allows reproducing at any point of the deposit, a similar complex thermal history. It considers the heat accumulation directly brought by the preheating, but also the one induced during the manufacturing process by layers overlapping. As pointed by LPBF1 and LPBF2 cases, constant melt pool increases the sample homogeneity. Achieving in addition close thermal histories along the sample depth yields the best hardness homogeneity as for sample LPBF2. It relies on high peak temperatures within the melt pool. The post mortem cracks phenomena in DED manufactured parts can also be avoided with these high temperatures as an in-situ annealing happens.

Adding within the cost function the need of a high average of peak temperature within the melt pool will be the next research step for this material. Ongoing work is being carried out to optimize the process parameters using machine learning strategies. Note that the thermal history predicted by solid FE simulations will not be able to explain the nanohardness variation within the melt pool

Published in : Optics & Laser Technology (2023), vol. 163, 109426
DOI: 10.1016/j.optlastec.2023.109426
Status : Postprint (Author's version)

zones. To this end, Marangoni effect should be added within the modelling though computational fluid mechanics and a higher mesh density.

CRediT authorship contribution statement

Rúben Tome Jardin: Software, Data curation, Investigation. **Victor Tuninetti:** Writing - original draft, Visualization, Formal analysis, Funding acquisition. **Jérôme Tchoufang Tchuindjang:** Formal analysis, Data curation. **Laurent Duchene:** Conceptualization, Methodology. **Neda Hashemi:** Software, Data curation. **Hoang Son Tran:** Software. **Raoul Carrus:** Validation. **Anne Mertens:** Conceptualization, Methodology. **Anne Marie Habraken:** Conceptualization, Supervision, Formal analysis, Writing - review & editing, Funding acquisition.

Declaration of Competing Interest

The authors declare that they have no known competing financial interests or personal relationships that could have appeared to influence the work reported in this paper.

Data availability

Data will be made available on request.

Acknowledgments

This work was funded by Walloon Region through the RW 11-1-7335 Recylclad project, FNRS F.R.S. [PDR T.0039.14], FEDER [IAWATHA], the cooperation agreement WBI/AGCID SUB2019/419031 (DIE19-0005) and Universidad de La Frontera (DI22-0067). As Research Director of FRS-FNRS, A.M.H. acknowledges the support of this institution. The Center for Applied Research and Education in Microscopy CAREM of ULiege is also thanked for providing SEM/EDS facilities. Computational resources were provided by the Consortium des Equipements de Calcul Intensif (CE^{é}CI) funded by the F.R.S.-FNRS. The authors also acknowledge Olivier Dedry for providing additional thermophysical properties data and Helene Morch for the improvement of the optimization method.

Appendix A. Supplementary material

Supplementary data to this article can be found online at https://doi.org/10.1016/j.optlastec.2023.109426.

Published in : Optics & Laser Technology (2023), vol. 163, 109426
DOI: 10.1016/j.optlastec.2023.109426
Status : Postprint (Author's version)

References

[1] P. Alvarez, M.A. Montealegre, F. Cordovilla, A. Garcia-Beltran, I. Angulo, J.

L. Ocana, Direct Generation of High-Aspect-Ratio Structures of AISI 316L by Laser- Assisted Powder Deposition, Materials (Basel). 13 (2020) 5670, https://doi.org/ 10.3390/ma13245670.

[2] C. Tan, J. Zou, S. Li, P. Jamshidi, A. Abena, A. Forsey, R.J. Moat, K. Essa, M. Wang, K. Zhou, M.M. Attallah, Additive manufacturing of bio-inspired multi-scale hierarchically strengthened lattice structures, Int. J. Mach. Tools Manuf. 167 (2021), 103764, https://doi.org/10.1016/j.ijmachtools.2021.103764.

[3] J. Huang, L. Qi, J. Luo, L. Zhao, H. Yi, Suppression of gravity effects on metal droplet deposition manufacturing by an anti-gravity electric field, Int. J. Mach. Tools Manuf. 148 (2020), 103474, https://doi.org/10.1016/j.

ijmachtools.2019.103474.

[4] A. Borovkov, L. Maslov, F. Tarasenko, M. Zhmaylo, I. Maslova, D. Solovev, Development of elastic-plastic model of additively produced titanium for personalised endoprosthetics, Int. J. Adv. Manuf. Technol. 117 (2021) 2117-2132, https://doi.org/10.1007/s00170-021-07460-1.

[5] D. Gu, X. Shi, R. Poprawe, D.L. Bourell, R. Setchi, J. Zhu, Material-structureperformance integrated laser-metal additive manufacturing, Science (80-.). 372 (2021). Doi: 10.1126/science.abg1487.

[6] C. Tan, F. Weng, S. Sui, Y. Chew, G. Bi, Progress and perspectives in laser additive manufacturing of key aeroengine materials, Int. J. Mach. Tools Manuf. 170 (2021), 103804, https://doi.org/10.1016/j.ijmachtools.2021.103804.

[7] D.-S. Shim, G.-Y. Baek, J.-S. Seo, G.-Y. Shin, K.-P. Kim, K.-Y. Lee, Effect of layer thickness setting on deposition characteristics in direct energy deposition (DED) process, Opt. Laser Technol. 86 (2016) 69-78, https://doi.Org/10.1016/j. optlastec.2016.07.001.

[8] N. Ur Rahman, L. Capuano, S. Cabeza, M. Feinaeugle, A. Garcia-Junceda, M.B. de Rooij, D.T.A. Matthews, G. Walmag, I. Gibson, G.R.B.E. Römer, Directed energy deposition and characterization of high-carbon high speed steels, Addit. Manuf. 30 (2019), 100838, https://doi.org/10.1016/j.addma.2019.100838.

[9] R.T. Jardin, V. Tuninetti, J.T. Tchuindjang, N. Hashemi, R. Carrus, A. Mertens, L. Duchene, H.S. Tran, A.M. Habraken, Sensitivity Analysis in the Modelling of a High Speed Steel Thin-Wall Produced by Directed Energy Deposition, Metals (Basel). 10 (2020) 1554, https://doi.org/10.3390/met10111554.

[10] S.J. Wolff, H. Wang, B. Gould, N. Parab, Z. Wu, C. Zhao, A. Greco, T. Sun, In situ X- ray imaging of pore formation mechanisms and dynamics in laser powder-blown directed energy deposition additive manufacturing, Int. J. Mach. Tools Manuf. (2021), https://doi.org/10.1016/j.ijmachtools.2021.103743.

[11] J.W. Murray, A. Speidel, A. Jackson-Crisp, P.H. Smith, H. Constantin, A.T. Clare, Unprocessed machining chips as a practical feedstock in directed energy deposition, Int. J. Mach. Tools Manuf. 169 (2021), 103803, https://doi.org/ 10.1016/j.ijmachtools.2021.103803.

[12] J.Y. Hascoet, S. Touze, M. Rauch, Automated identification of defect geometry for metallic part repair by an additive manufacturing process, Weld. World. (2018), https://doi.org/10.1007/s40194-017-0523-0.

Published in : Optics & Laser Technology (2023), vol. 163, 109426
DOI: 10.1016/j.optlastec.2023.109426
Status : Postprint (Author's version)

[13] H. Siva Prasad, F. Brueckner, J. Volpp, A.F.H. Kaplan, Laser metal deposition of copper on diverse metals using green laser sources, Int. J. Adv. Manuf. Technol. 107 (2020) 1559-1568, https://doi.org/10.1007/s00170-020-05117-z.

[14] G. Xu, C. Song, H. Zhang, H. Lu, D. Wu, K. Luo, J. Lu, Spatially heterogeneous microstructure in in-situ TiO-reinforced Ti6Al4V/316L functionally graded material fabricated via directed energy deposition, Addit. Manuf. 59 (2022), 103178, https://doi.org/10.1016/j.addma.2022.103178.

[15] H. Chen, Y. Chen, Y. Liu, Q. Wei, Y. Shi, W. Yan, Packing quality of powder layer during counter-rolling-type powder spreading process in additive manufacturing, Int. J. Mach. Tools Manuf. 153 (2020), 103553, https://doi.org/10.1016/j. ijmachtools.2020.103553.

[16] A. Malakizadi, T. Hajali, F. Schulz, S. Cedergren, J. Älgardh, R. M'Saoubi, E. Hryha, P. Krajnik, The role of microstructural characteristics of additively manufactured Alloy 718 on tool wear in machining, Int. J. Mach. Tools Manuf. 171 (2021), 103814, https://doi.org/10.1016/j.ijmachtools.2021.103814.

[17] S.M.H. Hojjatzadeh, N.D. Parab, Q. Guo, M. Qu, L. Xiong, C. Zhao, L.I. Escano, K. Fezzaa, W. Everhart, T. Sun, L. Chen, Direct observation of pore formation mechanisms during LPBF additive manufacturing process and high energy density laser welding, Int. J. Mach. Tools Manuf. 153 (2020), 103555, https://doi.org/10.1016/j.ijmachtools.2020.103555.

[18] T. Furumoto, S. Abe, M. Yamaguchi, A. Hosokawa, Improving surface quality using laser scanning and machining strategy combining powder bed fusion and machining processes, Int. J. Adv. Manuf. Technol. 117 (2021) 3405-3413, https:// doi.org/10.1007/s00170-021-07880-z.

[19] J. Lu, H. Lu, X. Xu, J. Yao, J. Cai, K. Luo, High-performance integrated additive manufacturing with laser shock peening -induced microstructural evolution and improvement in mechanical properties of Ti6Al4V alloy components, Int. J. Mach. Tools Manuf. 148 (2020), 103475, https://doi.org/10.1016/j.

ijmachtools.2019.103475.

[20] C. Wang, X.P. Tan, S.B. Tor, C.S. Lim, Machine learning in additive manufacturing: State-of-the-art and perspectives, Addit. Manuf. 36 (2020), 101538, https://doi. org/10.1016/j.addma.2020.101538.

[21] D. Carluccio, M. Bermingham, D. Kent, A.G. Demir, B. Previtali, M.S. Dargusch, Comparative Study of Pure Iron Manufactured by Selective Laser Melting, Laser Metal Deposition, and Casting Processes, Adv. Eng. Mater. 21 (2019) 1900049, https://doi.org/10.1002/adem.201900049.

[22] F. Soffel, D. Eisenbarth, K. Wegener, Effect of clad height, substrate thickness and scanning pattern on cantilever distortion in direct metal deposition, Int. J. Adv. Manuf. Technol. 117 (2021) 2083-2091, https://doi.org/10.1007/s00170-021- 06925-7.

[23] N. Hashemi, A. Mertens, H.M. Montrieux, J.T. Tchuindjang, O. Dedry, R. Carrus, J. Lecomte-Beckers, Oxidative wear behaviour of laser clad High Speed Steel thick deposits: Influence of sliding speed, carbide type and morphology, Surf. Coatings Technol. 315 (2017) 519-529, https://doi.org/10.1016/j.surfcoat.2017.02.071.

[24] R.T. Jardin, J. Tchoufang Tchuindjang, L. Duchene, H.-S. Tran, N. Hashemi, R. Carrus, A. Mertens, A.M. Habraken, Thermal histories and microstructures in Direct Energy Deposition of a High Speed Steel thick deposit, Mater. Lett. 236 (2019) 42-45, https://doi.org/10.1016/j.matlet.2018.09.157.

[25] D.-S. Shim, G.-Y. Baek, E.-M. Lee, Effect of substrate preheating by induction heater on direct energy deposition of AISI M4 powder, Mater. Sci. Eng. A. 682 (2017) 550-562, https://doi.org/10.1016/j.msea.2016.11.029.

Published in : Optics & Laser Technology (2023), vol. 163, 109426
DOI: 10.1016/j.optlastec.2023.109426
Status : Postprint (Author's version)

[26] S.M.J. Razavi, F. Berto, Directed Energy Deposition versus Wrought Ti-6Al-4V: A Comparison of Microstructure, Fatigue Behavior, and Notch Sensitivity, Adv. Eng. Mater. 21 (2019) 1900220, https://doi.org/10.1002/adem.201900220.

[27] R.A. Rahman Rashid, M.A. Javed, C. Barr, S. Palanisamy, N. Matthews, M.

5. Dargusch, Effect of in situ tempering on the mechanical, microstructural and corrosion properties of 316L stainless steel laser-cladded coating on mild steel, Int.

J. Adv. Manuf. Technol. 117 (2021) 2949-2958, https://doi.org/10.1007/s00170- 021-07886-7.

[28] T. Deng, J. Li, Z. Zheng, Fundamental aspects and recent developments in metal surface polishing with energy beam irradiation, Int. J. Mach. Tools Manuf. 148 (2020), 103472, https://doi.org/10.1016/j.ijmachtools.2019.103472.

[29] V. Tuninetti, G. Gilles, P. Flores, G. Pincheira, L. Duchene, A.M. Habraken, Impact of distortional hardening and the strength differential effect on the prediction of large deformation behavior of the Ti6Al4V alloy, Meccanica. 54 (2019) 1823-1840, https://doi.org/10.1007/s11012-019-01051-x.

[30] V. Tuninetti, P. Flores, M. Valenzuela, G. Pincheira, C. Medina, L. Duchene, A.- M. Habraken, Experimental characterization of the compressive mechanical behaviour of Ti6Al4V alloy at constant strain rates over the full elastoplastic range, Int. J. Mater. Form. 13 (2020) 709-724, https://doi.org/10.1007/s12289-020- 01543-2.

[31] Y. Su, Z. Wang, H. Lu, K. Luo, J. Lu, Improved wear resistance of directed energy deposited Fe-Ni-Cr alloy via closed-loop controlling laser power, J. Manuf. Process. 75 (2022) 802-813, https://doi.org/10.1016/j.jmapro.2022.01.047.

[32] Y. Su, Z. Wang, X. Xu, K. Luo, J. Lu, Effect of closed-loop controlled melt pool width on microstructure and tensile property for Fe-Ni-Cr alloy in directed energy deposition, J. Manuf. Process. 82 (2022) 708-721, https://doi.org/10.1016/j. jmapro.2022.08.049.

[33] W. Cong, F. Ning, A fundamental investigation on ultrasonic vibration-assisted laser engineered net shaping of stainless steel, Int. J. Mach. Tools Manuf. 121 (2017) 61-69, https://doi.org/10.1016/j.ijmachtools.2017.04.008.

[34] S.-H. Park, P. Liu, K. Yi, G. Choi, K.-Y. Jhang, H. Sohn, Mechanical properties estimation of additively manufactured metal components using femtosecond laser ultrasonics and laser polishing, Int. J. Mach. Tools Manuf. 166 (2021), 103745, https://doi.org/10.1016/j.ijmachtools.2021.103745.

[35] H. Tan, C. Zhang, W. Fan, F. Zhang, X. Lin, J. Chen, W. Huang, Dynamic evolution of powder stream convergence with powder feeding durations in direct energy deposition, Int. J. Mach. Tools Manuf. 157 (2020), 103606, https://doi.org/ 10.1016/j.ijmachtools.2020.103606.

[36] L. Peng, J. Shengqin, Z. Xiaoyan, H. Qianwu, X. Weihao, Direct laser fabrication of thin-walled metal parts under open-loop control, Int. J. Mach. Tools Manuf. 47 (2007) 996-1002, https://doi.org/10.1016/j.ijmachtools.2006.06.017.

[37] W. Woo, D.-K. Kim, E.J. Kingston, V. Luzin, F. Salvemini, M.R. Hill, Effect of interlayers and scanning strategies on through-thickness residual stress distributions in additive manufactured ferritic-austenitic steel structure, Mater. Sci. Eng. A. 744 (2019) 618-629, https://doi.org/10.1016/j.msea.2018.12.078.

[38] M. Biegler, J. Wang, L. Kaiser, M. Rethmeier, Automated Tool-Path Generation for Rapid Manufacturing of Additive Manufacturing Directed Energy Deposition Geometries, Steel Res. Int. 91 (2020), https://doi.org/10.1002/srin.202000017.

[39] T. Maurizi Enrici, O. Dedry, F. Boschini, J.T. Tchuindjang, A. Mertens, Microstructural and Thermal Characterization of 316L + WC Composite Coatings Obtained by Laser Cladding, Adv. Eng. Mater. 22 (2020) 2000291, https://doi.org/ 10.1002/adem.202000291.

[40] H.-S. Tran, J.T. Tchuindjang, H. Paydas, A. Mertens, R.T. Jardin, L. Duchene, R. Carrus, J. Lecomte-Beckers, A.M. Habraken, 3D thermal finite element analysis of laser cladding processed Ti-6Al-4V part with microstructural correlations, Mater. Des. 128 (2017) 130-142, https://doi.org/10.1016/j.matdes.2017.04.092.

[41] J.I. Arrizubieta, A. Lamikiz, M. Cortina, E. Ukar, A. Alberdi, Hardness, grainsize and porosity formation prediction on the Laser Metal Deposition of AISI 304 stainless steel, Int. J. Mach. Tools Manuf. 135 (2018) 53-64, https://doi.org/ 10.1016/j.ijmachtools.2018.08.004.

[42] J. Zhang, L. Yang, Z. Li, Q. Zhang, M. Yu, C. Fang, H. Xiao, Transport phenomenon, flow field, and deposition forming of metal powder in the laser direct deposition with designed nozzle, Int. J. Adv. Manuf. Technol. 114 (2021) 1373-1383, https:// doi.org/10.1007/s00170-021-06913-x.

[43] H. Lu, L. Wu, H. Wei, J. Cai, K. Luo, X. Xu, J. Lu, Microstructural evolution and tensile property enhancement of remanufactured Ti6Al4V using hybrid manufacturing of laser directed energy deposition with laser shock peening, Addit. Manuf. 55 (2022), 102877, https://doi.org/10.1016/j.addma.2022.102877.

[44] C. Rojas-Ulloa, C. Bouffioux, A.F. Jaramillo, C.M. García-Herrera, T. Hussain, L. Duchene, G. Riu, J. Josep Roa, P. Flores, A. Marie Habraken, V. Tuninetti, Nanomechanical Characterization of the Deformation Response of Orthotropic Ti-6Al-4V, Adv. Eng. Mater. (2021), https://doi.org/10.1002/adem.202001341.

[45] T. Guan, S. Chen, X. Chen, J. Liang, C. Liu, M. Wang, Effect of laser incident energy on microstructures and mechanical properties of 12CrNi2Y alloy steel by direct laser deposition, J. Mater. Sci. Technol. 35 (2019) 395-402, https://doi.org/ 10.1016/j.jmst.2018.10.024.

[46] K.M. Bertsch, G. Meric de Bellefon, B. Kuehl, D.J. Thoma, Origin of dislocation structures in an additively manufactured austenitic stainless steel 316L, Acta Mater. 199 (2020) 19-33, https://doi.org/10.1016/j.actamat.2020.07.063.

[47] Z. Zhang, Z. Liu, D. Wu, Prediction of melt pool temperature in directed energy deposition using machine learning, Addit. Manuf. 37 (2021), 101692, https://doi. org/10.1016/j.addma.2020.101692.

[48] T.Q.D. Pham, T.V. Hoang, X. Van Tran, Q.T. Pham, S. Fetni, L. Duchene, H.S. Tran, A.-M. Habraken, Fast and accurate prediction of temperature evolutions in additive manufacturing process using deep learning, J. Intell. Manuf. (2022), https://doi. org/10.1007/s10845-021-01896-8.

[49] T.Q.D. Pham, T.V. Hoang, X.V. Tran, S. Fetni, L. Duchene, H.S. Tran, A. M. Habraken, Characterization, propagation, and sensitivity analysis of uncertainties in the directed energy deposition process using a deep learning-based surrogate model, Probabilistic Eng. Mech. 69 (2022), 103297, https://doi.org/ 10.1016/j.probengmech.2022.103297.

[50] S. Cescotto, R. Charlier, Frictional contact finite elements based on mixed variational principles, Int. J. Numer. Methods Eng. 36 (1993) 1681-1701, https:// doi.org/10.1002/nme.1620361005.

[51] A.M. Habraken, S. Cescotto, Contact between deformable solids: The fully coupled approach, Math. Comput. Model. 28 (1998) 153-169, https://doi.org/10.1016/ S0895-7177(98)00115-0.

[52] S. Yuan, L. Duchene, C. Keller, E. Hug, C. Folton, E. Betaieb, O. Milis, A.- M. Habraken, Mechanical response of nickel multicrystals for shear and tensile conditions at room temperature and 573 K, Mater. Sci. Eng. A. 809 (2021), 140987, https://doi.org/10.1016/j.msea.2021.140987.

Published in : Optics & Laser Technology (2023), vol. 163, 109426
DOI: 10.1016/j.optlastec.2023.109426
Status : Postprint (Author's version)

[53] S. Yuan, L. Duchene, C. Keller, E. Hug, A.-M. Habraken, Tunable surface boundary conditions in strain gradient crystal plasticity model, Mech. Mater. 145 (2020), 103393, https://doi.org/10.1016/j.mechmat.2020.103393.

[54] MSM & GEG (ULiege), Lagamine software, Univ. Liege. (2022). http://www.lagamine.uliege.be/dokuwiki/doku.php (accessed April 12, 2022).

[55] S. Fetni, T.M. Enrici, T. Niccolini, H.S. Tran, O. Dedry, L. Duchene, A. Mertens, A. M. Habraken, Thermal model for the directed energy deposition of composite

coatings of 316L stainless steel enriched with tungsten carbides, Mater. Des. 204 (2021), 109661, https://doi.org/10.1016/j.matdes.2021.109661.

[56] B.A. Khamidullin, I.V. Tsivilskiy, A.I. Gorunov, A.K. Gilmutdinov, Modeling of the effect of powder parameters on laser cladding using coaxial nozzle, Surf. Coatings Technol. 364 (2019) 430-443, https://doi.Org/10.1016/j.surfcoat.2018.12.002.

[57] H. Yin, L. Wang, S.D. Felicelli, Comparison of two-dimensional and threedimensional thermal models of the LENS® process, J. Heat Transfer. 130 (2008) 1-7, https://doi.org/10.1115/1.2953236.

[58] H. Morch, L. Duchene, R. Harzallah, V. Tuninetti, A.M. Habraken, Efficient temperature dependence of parameters for thermo-mechanical finite element modeling of alloy 230, Eur. J. Mech. - A/Solids. 85 (2021), 104116, https://doi. org/10.1016/j.euromechsol.2020.104116.

[59] S. Qu, Y. Gong, Effect of heat treatment on microstructure and mechanical characteristics of 316L stainless steel parts fabricated by hybrid additive and subtractive process, Int. J. Adv. Manuf. Technol. 117 (2021) 3465-3475, https:// doi.org/10.1007/s00170-021-07786-w.